PHASED-ARRAY NEAR FIELD RADIOMETRY FOR BRAIN INTRACRANIAL APPLICATIONS

A. Oikonomou, I. S. Karanasiou, and N. K. Uzunoglu

Microwave and Fiber Optics Laboratory
National Technical University of Athens, Greece

Abstract—During the past decades there has been a tremendous increase throughout the scientific community for developing methods of understanding human brain functionality, as diagnosis and treatment of diseases and malfunctions, could be effectively developed through understanding of how the brain works. In parallel, research effort is driven on minimizing drawbacks of existing imaging techniques including potential risks from radiation and invasive attributes of the imaging methodologies. Towards that direction a new near field radiometry imaging system has been theoretically studied, developed and experimentally tested and all of the aforementioned research phases are herein presented. The system operation principle is based on the fact that human tissues emit chaotic thermal type radiation at temperatures above the absolute zero. Using a phase shifted antenna array system, spatial resolution, detection depth and sensitivity are increased. Combining previous research results, as well as new findings, the capabilities of the constructed system, as well as the possibility of using it as a complementary method for brain imaging are discussed in this paper.

1. INTRODUCTION

The present paper discusses the potential of a newly constructed prototype microwave radiometric system for use in intracranial diagnostic applications. Radiometry is based on the measurement of thermal electromagnetic, noise-type, radiation emanating from lossy media, at temperatures above the absolute zero.

In microwave frequencies it is possible to detect the radiation emitted by tissues up to several centimeters of depth from the body

surface. Research towards that direction has begun more than 30 years ago [1] and it still attracts many researchers and engineers. During the past decades a number of devices and systems have been implemented in both radiometric and hyperthermia applications [2–8], mainly for use in parallel with clinical diagnostic and therapeutic methods.

Despite the great awareness and interest of researchers for microwave radiometry most of the research is focused on breast imaging [9]. Brain imaging is considered a significantly more difficult application mainly due to the complexity as well as the structural, functional and electrical inhomogeneity of the human brain. Because of the above mentioned difficulties an effective applicator, able to scan the studied area of the tissue is needed in order to collect the radiation so that consequently the measurement results can be evaluated in practice. Moreover, near field radiometry due to its passive character can be an entirely non-aggravating complementary tool in several medical applications, such as hyperthermia treatment [10] or cancer detection [11, 12].

The thermal type radiation, emitted by the human body can be measured, by placing a number of receiving phased array antennas around the biological body. The signals are then measured and driven to a sensitive microwave receiver, a radiometer operating in the same frequency range.

In this paper, a newly developed phased array radiometric device is presented. The device is tested using numerous phantoms and results are compared with previous theoretical findings [13].

2. MATERIALS AND METHODS

2.1. Phased Array Radiometer

As already mentioned, the thermal type radiation is measured by placing the antennas around the subject. The received signals, after being digitally phase-shifted are combined and driven to a sensitive radiometric receiver.

The radiometer used for the proposed system was designed for the purposes of the present research and operates at central frequency $f_r = 3.2 \pm 0.45\,\text{GHz}$.

The receiver has four inputs one for each antenna used. Then there's a two stage low noise amplifier and a microwave strip-line band-pass filter which rejects the out of band spurious signals. The output is driven to a 6-bit low loss digital phase shifter in order to beam form the antenna patterns. There are four similar chains which are combined through a power combiner and the combined signal is amplified using another low noise amplifier. The final elements are a

linear power detector and a 16 bit analog to digital acquisition card. In this radiometer architecture, it is very important that all four chains are similar so there will be no need for any calibration. The whole system is remotely controlled via a computer interface. For that reason appropriate user friendly software developed in LabView is developed which controls the four microwave phase shifters and the acquisition of the final data.

Microstrip line technique was used for constructing both the amplifiers and the filters. The detector's linear operating region lies in the -50–0 dBm region. Therefore, in order to ensure signal detection, the amplified output before the final filtering stage must lie into this region, ideally at the center of the linear region. The latter prerequisite takes into account random losses that cannot be mathematically formulated and calculated beforehand but are expected to appear due to the multistage character of the designed radiometric receiver. In the present approach the estimation was of an extra 20 dB loss, an assumption that proves to be sufficient as numerical results will certify.

In radiometry, the equivalent temperature of a receiver is $T = 300$ K and the power in a receiver's input is

$$\text{Pin} = kTBN_f \tag{1}$$

where $k = 1.38 \times 10^{-23}$ J/K is Boltzmann's constant, $T = 300$ K, $B = 9 \times 10^8$ Hz is the radiometer's bandwidth and $N_f \approx 3.5$ dB, its noise figure. Therefore the power at the receiver's input, calculated in dBm, is:

$$\text{Pin} = 10 \log(kTBN_f) = -173.83 + 89.54 + 3.5 = -80.79 \, \text{dBm}$$

Consequently, the additional required gain from the amplifiers, given by the Equation (2),

$$\text{Pout} = \text{Pin} + \text{Gain} = -25 \, \text{dBm} \tag{2}$$

should be 55.79 dB.

The desired total gain is provided by two separate low noise amplifiers. The first is a two stage LNA with total gain of $G_1 \approx 40$ dB and is placed in front of each separate chain. The filter is decided to be placed after the LNA since the lowest noise possible is more crucial than the out of band rejection. A second stage amplification follows next with an LNA having gain of $G_2 = 20$ dB.

The most crucial part of the design is to ensure that the four input chains are identical, thus no calibration is required. The microware phase shifters are digitally controlled and can provide any phase difference on demand with a minimal step of

$$\Delta\phi = \frac{360°}{2^6} = \frac{360°}{64} = 5.625° \tag{3}$$

The individual receiver's circuits were simulated using commercially available software (Agilent Advanced Design System) and were printed on dielectric RO4350$^{\text{TM}}$. The desired phase shift is obtained using HMC648LP6 by Hittite Microwave Corp. [14]. The digital control of each elements phase shift provides better accuracy, whilst insertion losses remain below 0.5 dB.

The low noise amplifier used for the first amplification of the received signal of each chain is an MGA-86563 (Agilent Technologies$^{\text{TM}}$) with gain $G = 20$ dB and $NF = 1.6$ dB. As mentioned before the effort was to achieve a low noise factor at the beginning of the chain so as to maintain the overall noise figure of the system to low levels. The required bandpass filter was implemented by using a lowpass and a highpass filters with the desired cutoff frequencies (HFCN 3100 and LFCN 3400, Mini-Circuits$^{\text{TM}}$ respectively) [15]. The combination of these low loss amplifiers (1 dB and 2 dB respectively) allows out of band signal rejections with insignificant losses. Another LNA MGA-86563 is used before driving the signal to the phase shifter.

The amplified signal is then driven to the power combiner and the combined signal is once amplified by an LNA of gain $G = 20$ dB before driven to a bandpass filter to reject spurious and out of band signals.

The printed radiometer was placed in a metallic box, to ensure the isolation from external signals. SMA fasteners were placed outside the box so that the radiometer can be connected with the other devices, such as the antennas input and the PC. Its final size, after placing it into the metallic box is $14 \, \text{cm} \times 10 \, \text{cm}$. Taking into account the current development of all electronic parts involved, the effort was given to making the radiometer as small as possible so that it can be easily transferred. Initial tests showed that by using an additional amplifier placed very close to the antennas used the measurement sensitivity can be improved. For our experiments an LNA with $G = 18$ dB (ZRL-3500+, Mini Circuits) was placed between the antennas and the radiometer, allowing accurate measurements not only by using the designed LabView program but also with polymeters.

2.2. Patch Antennas

The appropriate antennas for the designed systems should fulfill a number of requirements small size, low cost as well as being sufficiently conformal in order to be placed around the head. Several versions of the designed antennas [16, 17] have been simulated and tested in order to achieve all requirements. The antennas used for the experiments are conformal patch antennas with resonance frequency of approximately $f = 3.1$ GHz and are connected to the radiometer via coaxial feed.

Though patch antennas can be easily manufactured it is not easy to combine high resonance frequency and sufficiently small size, as numerous research studies suggest [18–23]. The solution used in the proposed system is a small shorting pin placed at distance $d = 8$ mm from the patches' feed. Based on simulating results the feed is done at $r = 8$ mm from the antenna patch center. The smallest antenna that could fulfill all requirements was found to be 20 mm × 20 mm, manufactured on Rogers RO4350$^{\text{TM}}$, with dielectric constant $e_r = 3.66$ and thickness $= 0.762$ mm (Fig. 1).

The antenna was simulated using the finite element method and the predicted S_{11} was estimated to be slightly better than $S_{11} = -25$ dB at resonance frequency $f_r = 3.05$ GHz, whilst the bandwidth is approximately $B = 400$ MHz (Fig. 2).

In order to examine the actual response of the system a three-layered spherical head model is used. The skin is represented as a 2 mm-width spherical layer, whereas the skull is a 1 cm-width spherical shell and a sphere of radius 89 mm represents the brain gray and white matter area. The dielectric properties of each tissue at the system operation frequency are presented in Table 1 [24].
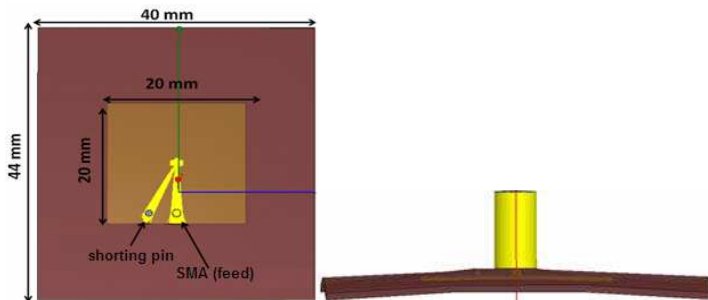
Figure 1. Patch antenna with shorting pin, design.
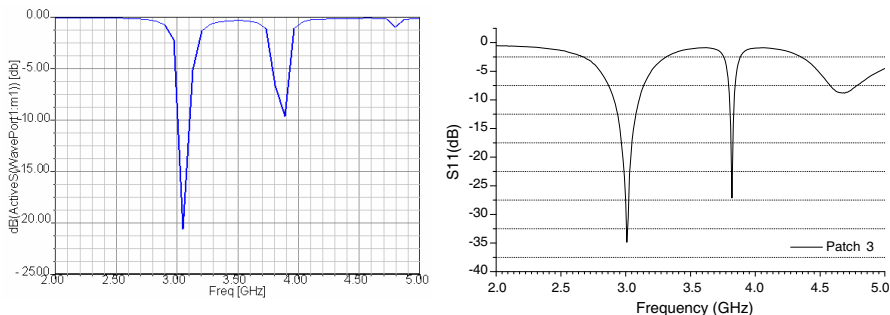
Figure 2. S_{11} (a) simulated, (b) experimental.

The estimated detection depth of each antenna is roughly $d = 3$ cm (2 cm inside the inner sphere that represents the brain), as can be seen in Fig. 3, where the normalized values of electric field are presented.

The research is concentrated on examining whether the system could provide reliable results by successfully monitoring a pre-specified brain area. To achieve this, it is essential to be able to observe a clear convergence of the antennas' directivity beams at each performed phase shift on the area of interest. Towards this direction, four identical antennas are modeled in the simulator environment, but having a different phase; each input signal is phase shifted in a cyclic way with $45°$ step. For example in the first trial of each antenna setup, the offset phase of the first antenna is $0°$, the offset phase of the second patch $45°$, the third $90°$ and the last $135°$. In the second trial of each setup, the phases are cyclically shifted resulting in a $135°$ offset phase for the first antenna, etc..

Simulated results, depicted in Fig. 4, confirm the improvement in the detection depth when using the phased array system, instead of a single antenna. The expected detection depth is improved approximately 67%, increasing the ability of the system to detect signals from regions up to $d = 5$ cm (4 cm inside the brain).

Circular alternation of each elements phase shows that the focal point of the system can be controlled based on each elements phase (Fig. 5).

Table 1. Tissues' dielectric properties.

Tissue	Permittivity	Conductivity
Avg. Brain	41.85	1.84
Avg. Skull	14.54	0.74
Skin (Dry)	37.47	1.72
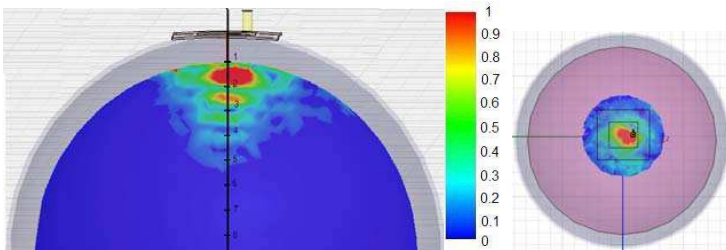
Figure 3. Electric field (a) transversal plane cut, (b) horizontal plane cut at depth from surface $d = 3$ cm.
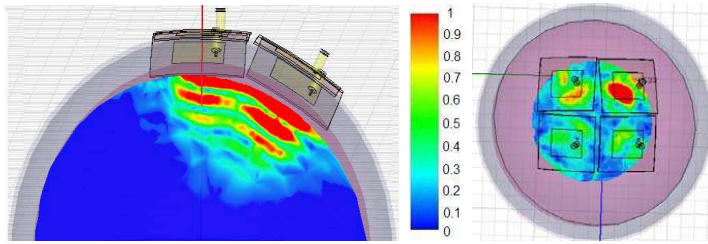
Figure 4. Electric field (a) transversal plane cut view, (b) horizontal plane cut at depth from surface $d = 5\,\text{cm}$.
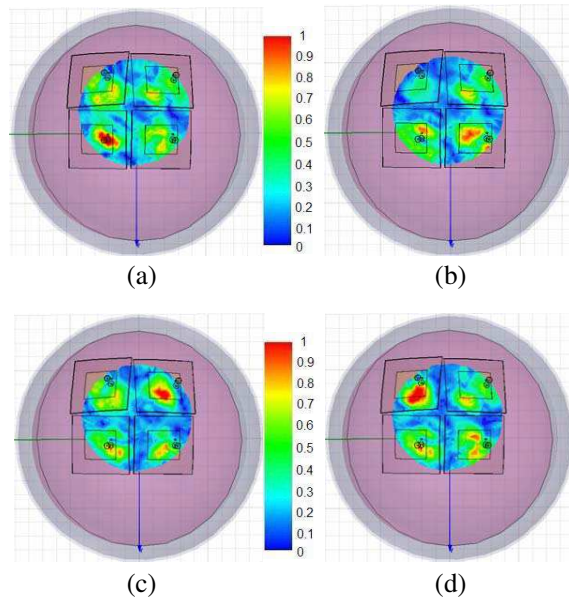
Figure 5. Phased array system in phases (horizontal cut plane at $d = 5\,\text{cm}$) (a) $0°$, $45°$, $90°$, $135°$. (b) $135°$, $0°$, $45°$, $90°$. (c) $90°$, $135°$, $0°$, $45°$ and (d) $45°$, $90°$, $135°$, $0°$.

3. EXPERIMENTAL PROCEDURES AND RESULTS

The radiometer is sensitive to external interference. To avoid measuring random electromagnetic waves and to eliminate the influence of external electromagnetic noise from other sources, all measurements took place into a Faraday chamber. Numerous tests have been carried out using water based phantoms in the form of cylindrical containers. The latter are placed in various positions relevant to each separate antenna element position, based on its phase.

Although the channels are identical and, thus, no differences were initially expected based on which antenna was in zero phase shift, in practice the latter affected the results. So, for each phase shift the base level and the sensitivity of the system are calculated.

The experimental setup consists of the radiometer and the antenna elements. The power supply is adjusted to 12 V and the radiometer is connected to a PC. A program in LabView controls the relevant phases whilst another program collects the data for further processing. The system is turned on and measurements are taken after approximately 20 min, a time window sufficient enough to provide stable baseline measurements.

Throughout the experiments distilled water based phantoms are used, therefore any variation in the measured output is a direct result of temperature and not conductivity variations [25]. Experimental procedures that investigate the system's capability to detect conductivity variations and therefore possible provide also information on brain functionality [25] will be reported elsewhere. In the present experiments, the temperature range under investigation covers 35–45°C, which is the typical range of temperatures with biological sense for the human body either due to internal mechanisms (e.g., normal temperature, fever) or due to external sources (e.g., hyperthermia treatment). A digital thermometer is used to accurately measure the phantom's temperature. All measurements are real-time measurements. The phantoms are not entirely thermally isolated. Thus, their temperature is measured throughout the experimental procedure, and the allowed temperature variation for every measurement does not exceed $\Delta\theta = 0.5$°C from the phantom's initial temperature.

3.1. Temperature Resolution

The first experiment is carried out using a small vessel with capacity 200 mL, containing warm water. Its initial temperature is 44°C. The phantom is placed in front of the antennas and remains still throughout the measurement. The temperature is measured using the electronic thermometer. Real time measurements are performed over a period of 40 sec, for each temperature. This period is calculated and limited by the fact that the container is not heat-insulated thus, there's rapid degradation of its temperature, especially at higher values. Separate sets of measurements are performed in the region 36–44°C with a step of 2°C. The average measured background noise throughout the experiment is $V_{bgrd} = 2.6587 \pm 0.0001$ V.

As it can be observed from Fig. 6, for $\Delta T = 8$°C, within the region of interest, the change of the measured output voltage range
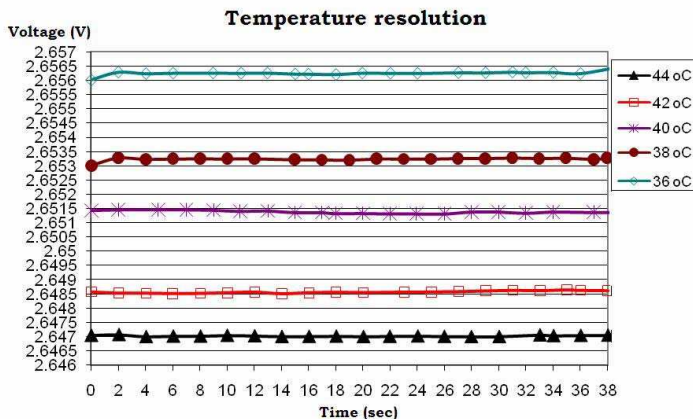
Figure 6. Radiometer's output at several temperatures.
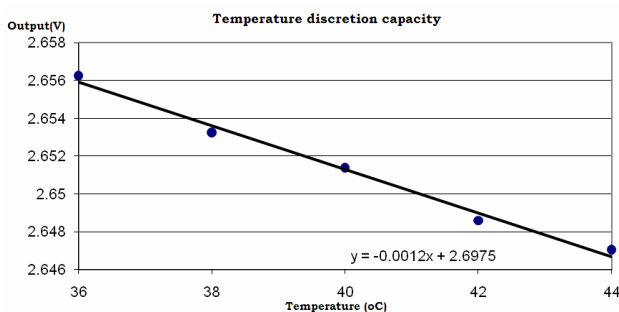
Figure 7. Mean value of received signal vs temperature.

is $\Delta V = 9.22\,\text{mV}$, leading to an average temperature resolution of $\frac{\Delta V}{\Delta T} = \frac{9.22\,\text{mV}}{8^\circ\text{C}} = 1,15\,\text{mV}/^\circ\text{C}$. If we calculate the average measured voltage output for each phantom's temperature, it can be easily observed that the correlation of the temperature and the radiometer's output is almost linear (Fig. 7).

The gradient of the optimal line is $1.2\,\text{mV}/^\circ\text{C}$. Combining this value with the temperature resolution we obtain:

$$\frac{1.15\,\text{mV}}{1.2\,\text{mV}/^\circ\text{C}} = 0.96^\circ\text{C} \tag{4}$$

3.2. Spatial Resolution — Focusing Area Determination

The second evaluation experiment determined the focusing abilities of the system. The experimental procedure used consists of the following steps:

1. Background measurements.
2. Measurement when the phantom is in front of the antenna with zero offset.
3. Measurements while the phantom is slowly moved from its initial. position towards the antenna with offset $\varphi = 45°$C.
4. Measurements when the phantom is in front of the antenna with offset $\varphi = 45°$C.

The same procedure as described in steps 2–4 was followed for offsets 90, and 135 and the experiment ended with a final background measurement.

Throughout the experiment a small spherical phantom of radius $r = 2$ cm is used. Its temperature lies in the middle of the temperature range of interest, around 40°C, at all cases.

The experiment was carried out for four discrete states of the system. It is important that the system has a uniform behavior regardless of which of the four antennas has zero offset (followed by circular change of the remaining offsets). Nevertheless, each antenna is considered "unique" and the variations of the received signal and/or background measurements are measured and examined.

When the antenna with zero offset is connected to the first channel, the presence of the phantom in front of it leads to a voltage drop of approximately $\Delta V = 12$ mV, when the phantom's temperature is approximately 40°C. Removal of the phantom from its initial position alters the measured output by approximately 4 mV. As can be seen in Fig. 8, from $t = 40$ s to $t = 60$ s, when the phantom is moving from one point to the other, the movement is immediately depicted in the receiver's input. In all cases, the movements from one antenna to the other are performed in 5 or 6 steps. When the phantom is displaced
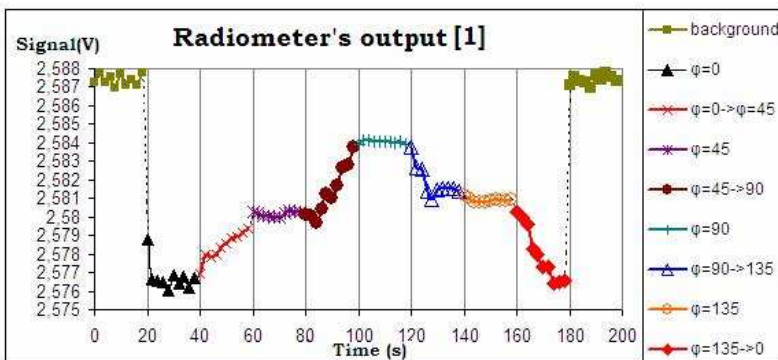
Figure 8. Output when the warm phantom is cyclic moving in front of the antennas with offsets: $\varphi_1 = 0°$, $\varphi_2 = 45°$, $\varphi_3 = 90°$, $\varphi_4 = 135°$.

by 5 mm, compared to the theoretical focus point, the output varies by 0.9 mV, while background variation is less than 0.2 mV throughout the experiment. If the phantom is placed further from the estimated focus point, under the antenna with $\varphi = 90°$ offset (which is the antenna placed the furthest from the focus point) we observe the output differences of $\Delta V = 8$ mV. The signal is strengthened again, once the phantom starts approaching the focus point, while moving towards the antenna with offset $\varphi = 135°$. The initial voltage drop of 12 mV is observed again when the phantom returns to the focus point under the antenna with zero offset.

The same procedure using different zero offset antenna is repeated. The results can be seen in Figs. 9–11.

As can be seen from all the experimental results a voltage drop reaches its maximum value, 12 mV, when the phantom is placed in front of the antenna connected to the channel with zero offset (2nd, 3rd and 4th respectively). When the phantom is placed in front of the antennas on either sides of the main one, the voltage drop, compared to the background, is 7–9 mV whilst it is increased by 3–5 mV compared to the signal received when the phantom is under to focus point. The weakest signal is received when the phantom remains under the antennas but in front of the furthest antenna, compared to its optimum spot. So, using sample initial measurements from the region of interest the phased array system can identify signal from a region of at least $r = 2$ cm. In Figs. 11–13, one can observe variations in the measured background signal as well as the signal received in the presence of the phantom in various places. All these can be eliminated, if using identical connection wires for all input elements.
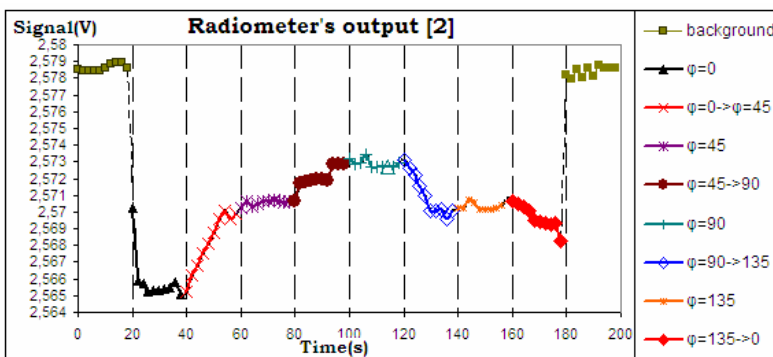
Figure 9. Output when the warm phantom is cyclic moving in front of the antennas with offsets $\varphi_1 = 135°$, $\varphi_2 = 0°$, $\varphi_3 = 45°$, $\varphi_4 = 90°$.
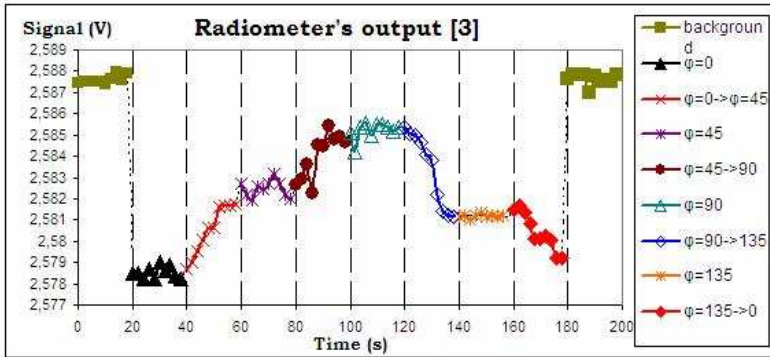
Figure 10. Output when the warm phantom is cyclic moving in front of the antennas with offsets $\varphi_1 = 90°$, $\varphi_2 = 135°$, $\varphi_3 = 0°$, $\varphi_4 = 45°$.
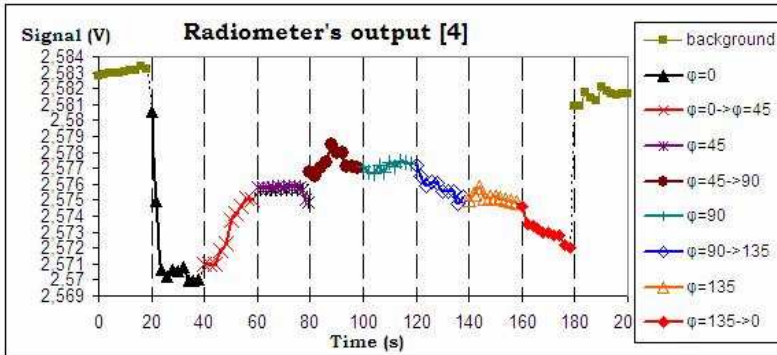
Figure 11. Output when the warm phantom is cyclic moving in front of the antennas with offsets $\varphi_1 = 45°$, $\varphi_2 = 90°$, $\varphi_3 = 135°$, $\varphi_4 = 0°$.

3.3. Spatial Resolution

In order to confirm the ability of the system to measure in-depth temperature changes a new phantom is used. It consists of a cylindrical vessel of radius $r = 8\,\mathrm{cm}$ containing sterilized water at room temperature, and a smaller one, having $r = 2\,\mathrm{cm}$, placed inside, at temperature $\Theta = 40°\mathrm{C}$. The protocol used is described below:

1. Background measurements.
2. Measurement when the phantom is at the focus point at depth $d = 0\,\mathrm{cm}$.

Steps 1 and 2 were replicated for $d = 1, 2, 3, 4, 5\,\mathrm{cm}$.

Throughout the experimental procedure background's variation never exceeded 0.007 mV. The phantom used is once more a spherical vessel of radius $r = 2$ cm containing sterilized water of temperature 42°C, placed into a larger container with sterilized water at room temperature. Besides the spatial resolution of the system exhibited with this experiment, the capability of the system to detect a warm area immersed in a cooler environment is also proved/shown.

As expected from Sections 1 and 2, when the small vessel is in front of the antenna connected to the channel with zero offset, an initial drop voltage of 15 mV is observed, comparing to free space (background) measurements. By placing the vessel at depth 1 cm the signal weakens by 2.5 mV. By placing the vessel in higher depths the signals weakens more, following an almost linear degradation, up to depth $d = 5$ cm, where it is invisible from the system (Fig. 12). By calculating the
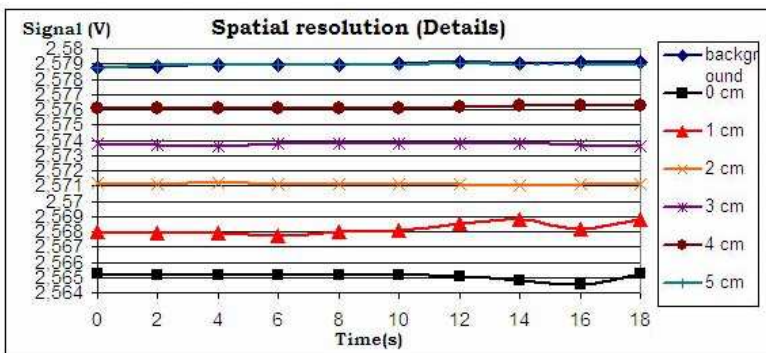
Figure 12. Receiver's signal — spatial resolution measurements.
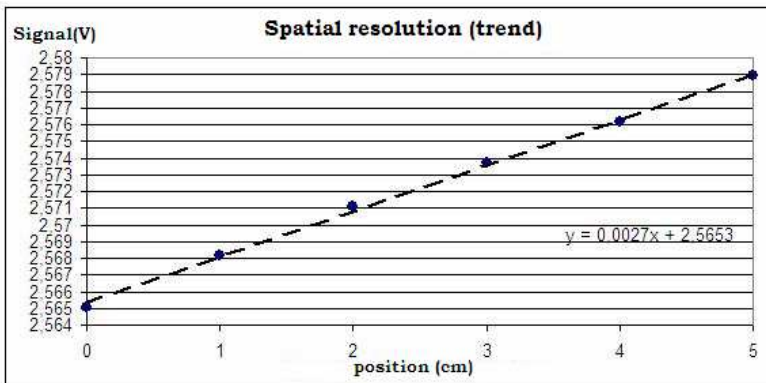
Figure 13. Receiver's signal vs phantom's place.

average received signal at each position we obtain Fig. 13, which verifies the linear behavior of the system. The gradient of the optimal line is $\Delta V/\Delta d = 2.7\,\mathrm{mV/cm}$. Based on this equation as well as theoretical simulations, it is expected that the system can identify small regions of higher temperature at depths up 4.5–5 cm in cylindrical water based phantoms.

4. DISCUSSION AND CONCLUSIONS

In the present paper the theoretical electromagnetic analysis, the design and implementation as well as the experimental results that verify the use of a novel portable phased array system are presented. Simulation results have shown that the proposed phased array system may provide detection of temperature changes in biological tissue for in-depth regions of up to 5 cm. A novel compact portable radiometric system with four inputs has been developed and its overall performance has been tested using phantoms. Extensive measurements have shown that by selecting appropriate phase shifts it is possible to identify a single focusing area in numerical and experimental phantoms. Experiments have shown that the system can identify different hot spots, as long as they are at least 1 cm apart, thus allowing reliable surface monitoring of in-depth tissues from surface antenna sensors via step measurements. The system's temperature resolution is less than 1°C. One of its advantages is that the focus point can be easily controlled via the phase shifting mechanism, which could render it a convenient tool for examining contiguous spots separated by 1 cm or more. The ability of identifying differences from regions of up to 4.5 cm inside the phantoms, separated by 1 cm, could make the system a valuable tool for use in cases where the exact location of the area of interest needs to be defined in an entirely passive manner. The system is small and can be easily transferred, while the antennas can easily be placed on any surface. Further investigation of its value during measurements with human volunteers and/or in conjunction with other noninvasive methods, such as near infrared spectroscopy could verify its contribution towards noninvasive, accurate results in the area of intracranial applications.

REFERENCES

1. Karanasiou, I. S., "Development of a non invasive brain imaging system using microwave radiometry," Doctor of Philosophy in Engineering, National Technical University of Athens, School of Electrical and Computer Engineering, Dec. 2003 (in Greek).

2. Jacobsen, S., P. R. Stauffer, and D. G. Neuman, "Dual-mode antenna design for microwave heating and noninvasive thermometry of superficial tissue disease," *IEEE Transactions on Biomedical Engineering*, Vol. 47, No. 11, 1500–1509, Nov. 2000.

3. Lee, J.-W., K.-S. Kim, S.-M. Lee, S.-J. Eom, and R. V. Troitsky, "A novel design of thermal anomaly for mammary gland tumor phantom for microwave radiometer," *IEEE Transactions on Biomedical Engineering*, Vol. 49, No. 7, 694–699, Jul. 2002.

4. Wang, C. R., L. P. Yan, Y. D. Deng, and C. J. Liu, "A double-armed planar equiangular spiral patch probe for biomedical measurements," *Journal of Electromagnetic Waves and Applications*, Vol. 22, No. 8–9, 1258–1266, 2008.

5. Gong, Y. and G. Wang, "Superficial tumor hyperthermia with flat left-handed metamaterial lens," *Progress In Electromagnetics Research*, Vol. 98, 389–405, 2009.

6. Drogoudis, D. G., G. A. Kyriacou, and J. N. Sahalos, "Microwave tomography employing an adjoint network based sensitivity matrix," *Progress In Electromagnetics Research*, Vol. 94, 213–242, 2009.

7. Lazaro, A., D. Girbau, and R. Villarino, "Simulated and experimental investigation of microwave imaging using UWB," *Progress In Electromagnetics Research*, Vol. 94, 263–280, 2009.

8. Iero, D., T. Isernia, A. F. Morabito, I. Catapano, and L. Crocco, "Optimal constraint field focusing for hyperthermia cancer therapy: A feasibility assessment on realistic phantoms," *Progress In Electromagnetics Research*, Vol. 102, 125–141, 2010.

9. Li, D., P. M. Meaney, and K. D. Paulsen, "Conformal microwave imaging for breast cancer detection," *IEEE Trans. on Microwave Theory and Techniques*, Vol. 51, 1179–1186, 2003.

10. Paulides, M. M., J. F. Bakker, and G. C. van Rhoon, "A patch antenna design for a phased-array applicator for hyperthermia treatment of head and neck tumours," *IEEE Transactions on Biomedical Engineering*, Vol. 54, No. 11, 2057–2063, Nov. 2007.

11. Rosen, A., M. Stuchly, and A. Vander Vorst, "Applications of RF/microwave in medicine, invited paper," *IEEE Trans. on Microwave Theory and Techniques*, Vol. 50, No. 3, 721–737, Mar. 2002.

12. Wang, Z., W. Che, and L. Zhou, "Uncertainty analysis of the rational function model used in the complex permittivity measurement of biological tissues using pmct probes within a wide microwave frequency band," *Progress In Electromagnetics Research*, Vol. 90, 137–150, 2009.

13. Gupta, K. C. and A. Benalla, *Microstip Antenna Design*, Artech House, 1988.

14. HMC648LP6 Datasheet by Hittite Microwave Corporation.

15. HFCN 3100 and LFCN 3400 datasheets, Mini-Circuits^{TM}.

16. Oikonomou, A., I. S. Karanasiou, and N. K. Uzunoglu, "Conformal phased array antennas for human brain imaging using near field radiometry," *URSI 2007*, Ottawa, Canada, Jul. 22–26, 2007.

17. Oikonomou, A. T., I. S. Karanasiou, and N. K. Uzunoglu, "Potential brain imaging using near field radiometry," *Journal of Instrumentation*, Vol. 4, 2009.

18. Yang, S. S., K.-F. Lee, A. A. Kishk, and K.-M. Luk, "Design and study of wideband single feed circularly polarized microstrip antennas," *Progress In Electromagnetics Research*, Vol. 80, 45–61, 2008.

19. Yin, X.-C., C.-L. Ruan, C.-Y. Ding, and J.-H. Chu, "A compact ultra-wideband microstrip antenna with multiple notches," *Progress In Electromagnetics Research*, Vol. 84, 321–332, 2008.

20. Mahmoud, S. F. and A. R. Al-Ajmi, "A novel microstrip patch antenna with reduced surface wave excitation," *Progress In Electromagnetics Research*, Vol. 86, 71–86, 2008.

21. Ansari, J. A., P. Singh, S. K. Dubey, R. U. Khan, and B. R. Vishvakarma, "H-shaped stacked patch antenna for dual band operation," *Progress In Electromagnetics Research B*, Vol. 5, 291–302, 2008.

22. Yu, Z.-W., G.-M. Wang, X.-J. Gao, and K. Lu, "A novel small-size single patch microstrip antenna based on koch and sierpinski fractal-shapes," *Progress In Electromagnetics Research Letters*, Vol. 17, 95–103, 2010.

23. Liu, X. F., Y. C. Jiao, and F. S. Zhang, "Conformal array antenna design using modified particle swarm optimization," *Journal of Electromagnetic Waves and Applications*, Vol. 22, No. 2–3, 207–218, 2008.

24. Gabriel, S., R. W. Lau, and C. Gabriel, "The dielectric properties of biological tissues: II. Measurements in the frequency range 10 Hz to 20 GHz," *Phys. Med. Biol.*, Vol. 41, 2251–2269, 1996.

25. Karanasiou, I. S., N. K. Uzunoglu, and A. Garetsos, "Electromagnetic analysis of a non-invasive 3D passive microwave imaging system," *Progress In Electromagnetic Research*, Vol. 44, 287–308, 2004.